Covariability of Near-Surface Wind Speed Statistics and Mesoscale Sea Surface Temperature Fluctuations

Johannes Gemmrich and Adam Monahan

March 2018

Covariability of Near-Surface Wind Speed Statistics and Mesoscale Sea Surface Temperature Fluctuations

JOHANNES GEMMRICH

Department of Physics and Astronomy, University of Victoria, Victoria, British Columbia, Canada

ADAM MONAHAN

School of Earth and Ocean Sciences, University of Victoria, Victoria, British Columbia, Canada

(Manuscript received 5 September 2017, in final form 22 December 2017)

ABSTRACT

The atmospheric (ABL) and ocean (OBL) boundary layers are intimately linked via mechanical and thermal coupling processes. In many regions over the world's oceans, this results in a strong covariability between anomalies in wind speed and SST. At oceanic mesoscale, this coupling can be driven either from the atmosphere or the ocean. Gridded SST and wind speed data at 0.25° resolution show that over the western North Atlantic, the ABL mainly responds to the OBL, whereas in the eastern North Pacific and in the Southern Ocean, the OBL largely responds to wind speed anomalies. This general behavior is also verified by in situ buoy observations in the Atlantic and Pacific. A stochastic, nondimensional, 1D coupled air–sea boundary layer model is utilized to assess the relative importance of the coupling processes. For regions of little intrinsic SST fluctuations (i.e., most regions of the world's oceans away from strong temperature fronts), the inclusion of cold water entrainment at the thermocline is crucial. In regions with strong frontal activities (e.g., the western boundary regions), the coupling is dominated by the SST fluctuations, and the frontal variability needs to be included in models. Generally, atmospheric and ocean-driven coupling lead to an opposite relationship between SST and wind speed fluctuations. This effect can be especially important for higher wind speed quantiles.

1. Introduction

Many regions of the world's oceans show a significant correlation between SST anomalies and wind speed anomalies ΔU. The sign and magnitude of this correlation is scale dependent (Chelton and Xie 2010) and also affected by the geographic location. At synoptic scales [O(1000 km)], the temperature of the ocean boundary layer (OBL) mainly responds to changes in sensible and latent heat fluxes, implying a strong negative correlation in mid- and high latitudes and a weak correlation in the tropics. At these large scales, the coupling is one way, such that the atmospheric boundary layer (ABL) forces the OBL. That is, wind speed fluctuations affect air–sea heat fluxes, and the high thermal inertia of the OBL acts as a low-pass filter to the atmospheric forcing, occurring at the higher-frequency ''weather'' time scale (Hasselmann 1976). Synoptic- to basin-scale SST anomalies are persistent for time scales that allow the air temperature to adjust and, therefore, can provide a weak negative feedback to the atmospheric forcing. This feedback strengthens with decreasing spatial scale of the SST anomaly (Frankignoul 1985). These processes are now well documented in observational studies and implemented in stochastic climate models [see the review in Bishop et al. (2017)].

On the other hand, at oceanic mesoscales (i.e., spatial scales of a few tens of kilometers and time scales of order a few hours to a few days), the ocean forces the atmosphere, and the correlation between SST anomalies and ΔU can be positive (Small et al. 2008). Here, we show that at these smaller spatial scales, the two boundary layers are governed by a two-way coupling, which can result in correlations of either sign.

In the case where the coupling is driven by the ocean side, positive correlations prevail, and the most direct effects are (i) the dependence of the ABL height on its stratification and (ii) the generation of horizontal pressure gradients. Positive SST anomalies create unstable ABL conditions, which leads to an increase in ABL height. This deepening of the ABL allows for an

Corresponding author: Johannes Gemmrich, gemmrich@uvic.ca

DOI: 10.1175/JPO-D-17-0177.1

enhanced downward flux of horizontal momentum and, thus, an increase in near-surface wind speed U. Similarly, for a given near-surface wind, the turbulent momentum flux difference between the surface and the top of the ABL is independent of the ABL depth. The mean turbulent momentum flux divergence is, therefore, inversely proportional to the ABL depth, again resulting in higher wind speeds associated with a deepening ABL. The second mechanism assumes that SST anomalies force an anomaly in the near-surface air temperature and moisture. The resulting horizontal density gradient implies a horizontal gradient in hydrostatic pressure and acceleration of the horizontal wind over the warm section. For an overview of the coupling processes and a detailed reference list, see, for example, Small et al. (2008).

The dynamically relevant quantity for the air–ocean system is the wind stress τ_A, rather than the wind speed. Under neutral ABL stratification, wind stress has a quadratic dependence on wind speed $\tau_A = C_D\rho u^2$, where ρ is the density of air, and C_D is the drag coefficient. However, the drag coefficient is larger under unstable conditions than under stable conditions. Therefore, the enhancement of the wind stress over positive SST anomalies is even greater than one would assume based on the wind speed dependence alone. This effect has implications, for example, for calculating vertical OBL velocities associated with Ekman pumping (Gaube et al. 2015), the computation of air–sea exchange processes (Fairall et al. 2003), the modeling of surface waves (Cavaleri et al. 2007), and the interpretation of remote sensing products from synthetic aperture radar (SAR) and scatterometers (Liu et al. 2016).

The processes discussed above yield an increase of wind speed over regions of warm water and, similarly, a decrease over colder sections, driven by the ocean side. This positive coupling is, to our knowledge, the only SST–wind speed coupling at mesoscale discussed in the literature. However, as we will describe in this paper, there is also a negative covariation at these smaller scales, especially in open ocean regions away from strong eddy activities. In these regions, the coupling is driven by the atmosphere, similar to what is observed at synoptic scales.

Here, we analyze the SST–ΔU dependencies (i.e., variations in the wind speed distribution conditioned on SST) from global wind and SST fields. In addition to the instantaneous dependence, we also discuss lagged correlation to extract the underlying physical mechanisms. The importance of these processes is further analyzed with an idealized 1D coupled air–sea boundary layer model.

2. Observations

This study assesses the coupling between anomalies in wind speed and SST on a scale of a few tens of kilometers and time scales of several hours to a few days. Therefore, we require collocated observations of wind and SST at these temporal and spatial scales. Here, we will analyze gridded products based on remote sensing data, as well as in situ buoy observations.

The gridded data have global daily coverage and $0.25° \times 0.25°$ spatial resolution. Wind speed $U = (u^2 + v^2)^{1/2}$ is calculated from the zonal (u) and meridional (v) wind components taken from the QuikSCAT Level 3 dataset (Perry 2001). These wind speeds are equivalent neutral winds obtained from remotely sensed estimates of surface stress. SST data are the blended Group for High Resolution Sea Surface Temperature (GHRSST) Level 4 data, incorporating an optimal interpolation of Advanced Very High Resolution Radiometer (AVHRR), Advanced Microwave Scanning Radiometer for Earth Observing System (AMSR-E), and in situ ship and buoy observations. This SST product is representative of the temperature at about 0.3-m depth (Reynolds et al. 2007). The period common to both datasets is June 2002 to November 2009.

We select three regions with similarly strong variability in wind speed but differing SST variability (Fig. 1): the western North Atlantic (34.875°–55.375°N, 47.75°–72.75°W), the eastern North Pacific (29.875°–49.875°N, 137.75°–175.25°W), and the Southern Ocean (47.625°–58.875°S, 32.5°E–85.25°W), with SST variability being strong, moderate, and weak, respectively.

In addition, we analyze in situ data of SST and wind speed from meteorological buoys, operated by Environment and Climate Change Canada, covering the same time span as the remote sensing data. The main purpose of these buoys is to measure the sea state, but they also record hourly wind speed and direction, as well as air and water temperature. Suitable buoys in our regions are C44137, C44138, C44140, C44142, and C44150 in the Atlantic and C46004, C46036, and C46184 in the Pacific (Fig. 1). There are no buoys in the Southern Ocean region. To get a regional perspective, all data from all buoys within the region are combined.

A coupling between the heat content of the oceanic surface layer and the momentum in the atmospheric boundary layer implies statistical dependence between SST anomalies and wind speed anomalies, ΔSST and ΔU. These anomalies are calculated for each grid point and each time step as the difference between the data point and the monthly mean from all years at the grid point. Although anomalies are calculated with respect to the monthly mean, these values are then combined into a seasonal subgroup. The monthly means at the grid points are spatially correlated, and, thus, the method of calculating the anomalies implies a spatial high-pass filtering of the data that yields local anomalies.

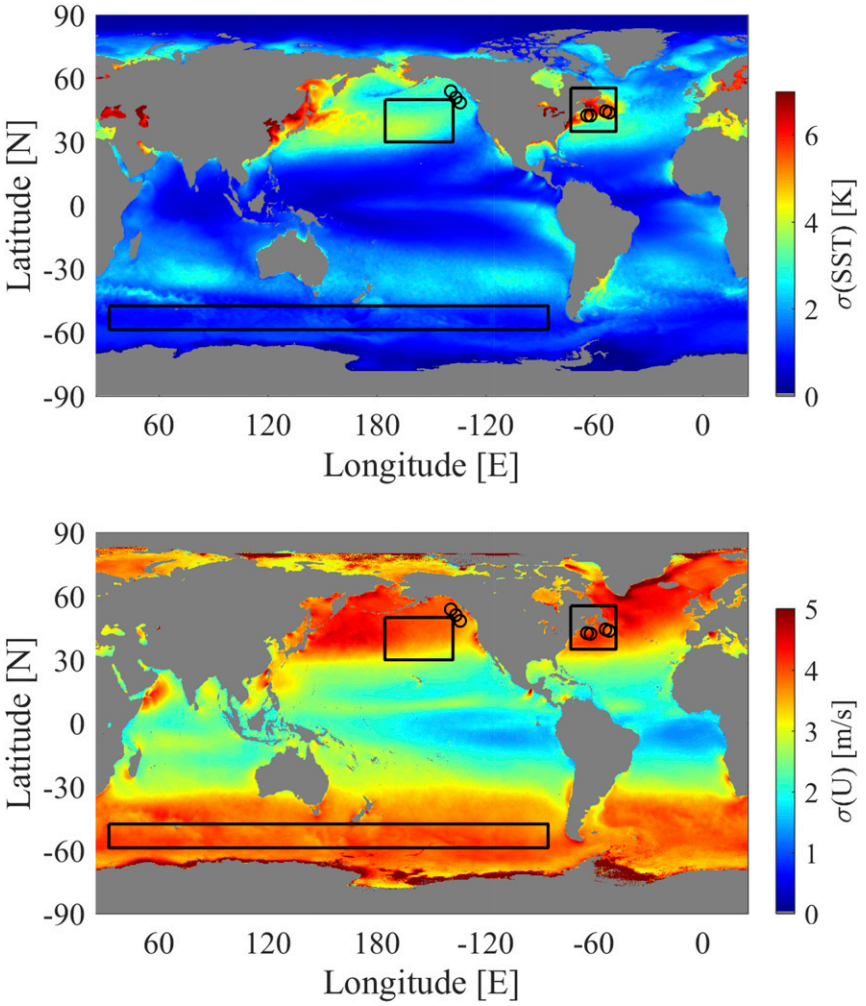

FIG. 1. Standard deviation of (top) SST and (bottom) wind speed from all gridded data. Black rectangles mark the three regions analyzed in detail, and black circles mark the location of buoys analyzed.

Only the wind speed, independent of direction, is considered in this analysis, and no attempt is made to extract spatial orientation of individual SST anomalies. The downwind component and crosswind component of SST gradients affect the wind field differently (see Chelton and Xie 2010); however, in a meandering front or over large areas, both responses are expected to occur roughly equally. Similarly, processes affecting the wind speeds other than SST anomalies, like strong ocean currents (Renault et al. 2016), are not considered.

3. Wind speed variations conditioned on ΔSST

For each region, all SST anomalies for a given season are divided into seven equal-sized quantile bins, and the wind speed anomalies corresponding to the same grid points (or same buoy) and same times are found. The individual bins are simply represented by the mean value of the SST anomalies within the bin. For the wind speed anomaly, we use three different measures, namely, the mean value, the 95th percentile, and the standard deviation σ, calculated from all daily data within a specific season. These datasets provide the instantaneous wind speed statistics conditioned on fluctuations in SST. The response of the ABL to SST variations might be delayed, and therefore, we also extract the wind speed anomalies at the same location, but with a delay $\tau > 0$. On the other hand, fluctuations in wind speed can cause anomalies in SST, which will also result in a lagged dependence, but with $\tau < 0$. Here, we consider the cases $\tau = [-5, -1, 0, 1, 5]$ d.

In all three regions, we find nearly linear dependencies between SST anomalies and wind speed changes. However, the strength and even the sign of this

relationship vary widely, depending on the region and the season (Figs. 2–4.)

a. Gridded data

In the Pacific region, the range of SST fluctuations is about ±2.5 K, with somewhat smaller values in the spring months. There is generally a negative correlation between wind speed statistics and SST (Fig. 2). The steepest slope is at negative lag, implying that the SST is responding to fluctuations in wind speed. As discussed above, the cooling of the OBL could be caused by a strong latent heat flux or a positive sensible heat flux associated with cold air. However, air–sea temperature and humidity differences over the northeast Pacific are commonly small and increased wind speeds would have only a weak effect on the heat flux (Yu and Weller 2007). Therefore, a more likely explanation for the reduction of SST following an increase in wind speed is enhanced entrainment of cooler water at the bottom of the OBL due to enhanced mixing. The magnitude of SST changes due to entrainment depends on the depth of the mixed layer, as well as the temperature difference across the base of it. Thus, a given wind speed anomaly will result in a weak SST response in early spring, when the mixed layer is deep and cold, and the strongest SST response is expected at the end of summer, when the mixed layer is shallow and its temperature differs the most from the layers below. This seasonal variability of mixed layer temperature response to atmospheric forcing observed in situ at Station Papa (50°N, 145°W) (Alexander and Penland 1996) is consistent with the weakest response in MAM and the strong response in JJA obtained in our analysis (Fig. 2).

A weak positive SST–wind speed covariability is observed for the longest lag $\tau = 5$ d in MAM, JJA, and SON when SST leads the changes in wind speed (i.e., increases in SST lead a slight increase in wind speed 5 days later). However, this signal is much weaker than the opposite signal of wind fluctuations leading SST anomalies throughout the entire year. The conditional standard deviation $\sigma(\Delta U)$ decreases with ΔSST, particularly for more negative lags, consistent with processes in which the atmosphere drives the ocean (e.g., enhanced wind speed variability results in enhanced mixing in the OBL). For positive lags, the slope is more or less flat. The extreme wind fluctuations, represented by the 95th percentile of the wind fluctuations in a given SST bin, show a conditional dependence behavior nearly identical to the ΔU_{mean}. The mean values of $\Delta U_{95\text{prct}}$ are 6.4 m s^{-1} in winter and drop to 4.2 m s^{-1} in summer.

In the Atlantic region, the relation between SST fluctuations and wind speed is more variable than in the Pacific region (Fig. 3). At positive lags, (i.e., ΔSST leads ΔU_{mean}), increased ocean temperature results in an increased wind

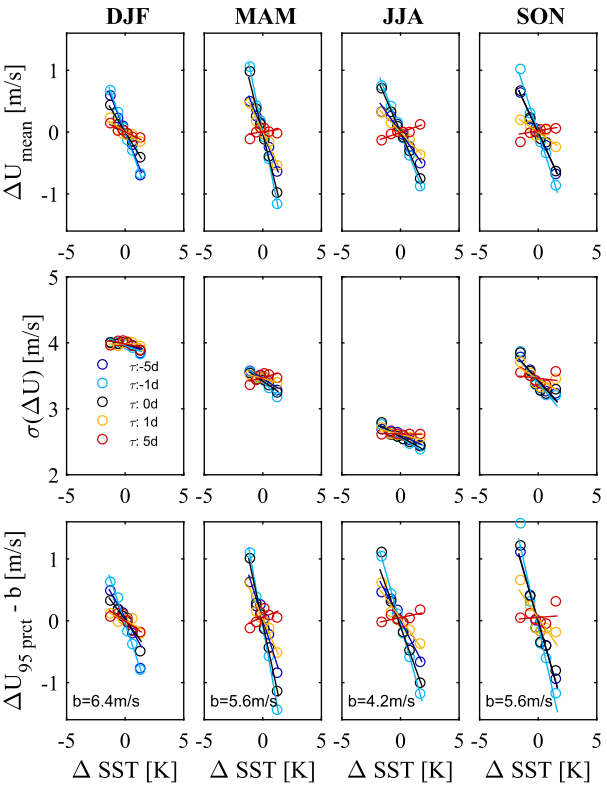

FIG. 2. Wind speed anomalies as a function of SST anomalies from gridded data products in the northeast Pacific for different lags τ. Individual data (circles) and least squares fit (line) are given for different lags. (top) Mean of wind speed anomalies; (middle) standard deviation of wind speed anomalies; (bottom) the 95th percentile of wind speed anomalies, offset by their mean value b.

speed, whereas at lags $\tau \leq 0$, increased wind speeds lead to a reduced SST, except during DJF. In other words, the sign of the correlation changes depending on whether the system is thermally ($\tau > 0$) or mechanically driven ($\tau < 0$). In this region, mesoscale ocean eddies in the meandering Gulf Stream create strong temperature fluctuations, independent of direct atmospheric driving. Thus, the ABL is regularly exposed to strong SST fluctuations that are not caused by local atmospheric processes. In turn, the modulation of the ABL stability results in a speed up (slow down) over positive (negative) SST fluctuations. On the other hand, the mechanical coupling (when ΔU_{mean} leads ΔSST) suggests that increased wind speed causes increased sensible and latent heat loss of the OBL, as well as cooling due to mixed layer deepening. The negative feedback is absent in the mean anomalies during the winter months. This is surprising, since continental outflow of cold and dry air masses will cause $\Delta\text{SST} < 0$ associated with $\Delta U > 0$, especially in winter. These outflow events dominate the overall heat flux but are rather infrequent (Shaman et al. 2010). Thus, we hypothesize that they mainly cause large

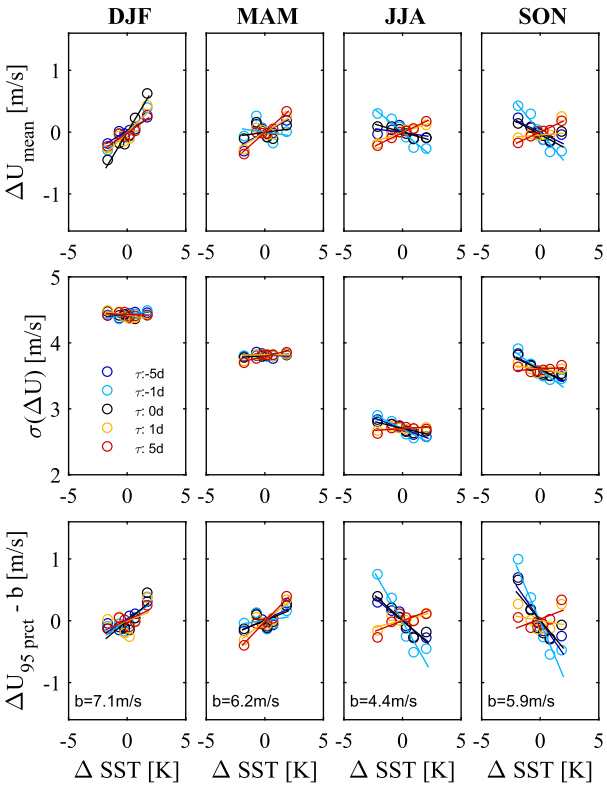

FIG. 3. As in Fig. 2, but for the northwest Atlantic.

SST anomalies and contribute to the high standard deviation seen for DJF. The weak positive average covariability results from the more frequent conditions of airflow from the southeast, where advection of warm and moist air precedes an increase in SST. Furthermore, entrainment and cooling of the OBL associated with higher wind speeds is less effective in this period of a generally deep OBL.

Overall, the air–sea coupling in this Atlantic region is dominated by thermal dynamics, with average SST fluctuations being about ±3 K. The standard deviation of the wind speed fluctuations is similar to that observed in the Pacific region. In contrast to the ΔSST–ΔU_{mean} dependence, the slope of ΔSST–$\sigma(\Delta U)$ is always negative, albeit small. The strongest negative slope is found for $\tau < 0$ in JJA and SON, indicating that wind speed variability has more of an effect on SST when the OBL is relatively shallow. The conditional standard deviation of ΔU is essentially independent of ΔSST in DJF when the system is dominated by thermal coupling. The extreme wind speed fluctuations are slightly smaller than what is found in the Pacific region. During JJA and SON, there is also a change of sign in the ΔSST–$\Delta U_{95\mathrm{prct}}$ correlation between $\tau < 0$ and $\tau > 0$, but for the extreme wind fluctuations, the signal of the mechanically driven coupling ($\tau < 0$) is stronger than the thermal coupling ($\tau > 0$), which is not the case for the mean wind fluctuations. Thus, the destabilization of the ABL by a given SST anomaly leads to a moderate increase of the extreme values of wind fluctuations (Sampe and Xie 2007), and the increased entrainment within the OBL associated with extreme wind speeds leads to a more pronounced covariability of wind speed and SST.

The coupling of the oceanic and atmospheric boundary layers in the Southern Ocean is mainly dominated by mechanical wind forcing (Fig. 4). This is similar to the situation in the northeast Pacific, but with weaker temperature variations of the OBL, likely due to the generally deeper OBL in the Southern Ocean: ΔSST = ±1 K and $-1.5 < \Delta U_{\mathrm{mean}} \leq 1\,\mathrm{m\,s^{-1}}$. Mean wind fluctuations are smallest during the austral winter, with $\Delta U_{\mathrm{mean}} \approx \pm 0.5\,\mathrm{m\,s^{-1}}$. Furthermore, this is the only season with a positive correlation for $\tau = 1$ d (i.e., a warming of the OBL leads to a slightly increased wind speed the next day). The seasonality of the conditional standard deviation of ΔU is much smaller than in the Pacific or Atlantic. Similarly, the extreme winds, which show the same SST–U correlations as the mean wind fluctuations, generally span a smaller range than their counterparts in the northern regions.

The Southern Ocean is a region of generally high wind speeds and a deep OBL, and fluctuations in wind speed mainly affect the air–sea heat flux, rather than modified entrainment. Air–sea heat fluxes in the Southern Ocean are generally upward, dominated by the latent heat flux (Schulz et al. 2012), and an increase in wind speed will lead to a lower SST, as observed.

Figures 2–4 suggest that the coupling between the atmospheric and oceanic boundary layers results in nearly linear dependencies between SST and the wind speed statistics considered, albeit with varying sign and strength. These variations for the conditional mean and 95th-percentile wind speed are respectively summarized by the slopes of the linear best fits $\Delta U_{\mathrm{mean}} = p_{\mathrm{mean}}\Delta\mathrm{SST} + c_1$ and $\Delta U_{95\mathrm{prct}} = p_{95\mathrm{prct}}\Delta\mathrm{SST} + c_2$ as functions of region, season, and lag (Fig. 5). In all three regions, the strongest coupling between SST and wind speed occurs at short lags $-1 \leq \tau \leq 1$ d (i.e., the response to changes occurs within about 1 day) independent of the source of the fluctuation. The strength of the coupling, $|p_{\mathrm{mean}}|$ and $|p_{95\mathrm{prct}}|$, can change by a factor of 2 between the different seasons. In the Pacific and the Southern Oceans, where the coupling is predominantly mechanical, the maximum occurs in the local spring and summer, respectively. In the Atlantic region, the strongest coupling is thermally driven ($p > 0$) and happens in winter and spring, whereas the strongest mechanical coupling ($p < 0$) occurs in fall. As discussed above, the Atlantic region shows a consistent positive correlation with SST leading conditional wind speed. The other observation of a positive correlation is in the Southern Ocean in the

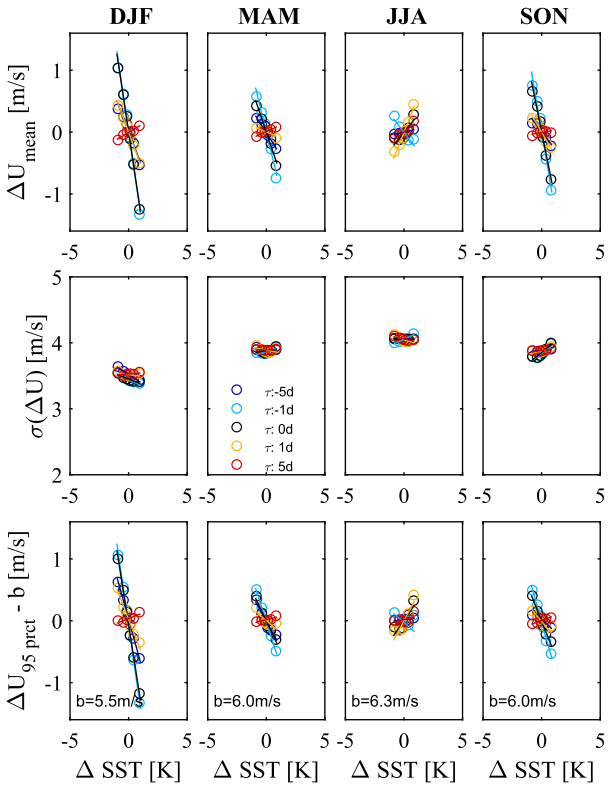

FIG. 4. As in Fig. 2, but for the Southern Ocean.

austral winter. Correlation between SST and extreme wind speed fluctuations generally shows the same features as the results for the mean wind speed fluctuations. In the Atlantic, generally, the response related to the extreme wind events is stronger than that related to the mean winds, $|p_{\text{mean}}| < |p_{95\text{prct}}|$; in the Pacific and the Southern Oceans, both are of similar strength.

A recent study by Seo (2017) gives a global map of correlation between SST and wind speed based on the same high-resolution gridded data, but zonally high-pass filtered at a cutoff corresponding to 10° to remove the correlation at synoptic scales. Results are given for zero lag and data for June–September. In the Atlantic region and the Southern Ocean, the filtered data show a strong positive correlation, and in the North Pacific, there is a weak negative correlation. These results are similar to ours only for the Southern Ocean, whereas we find a weak (strong) negative correlation for the Atlantic (Pacific) regions (Fig. 5; $\tau = 0$). Thus, in regions with small SST variability, like the Southern Ocean (Fig. 1), the ΔSST–wind speed covariability remains the same over a wide range of spatial scales. However, in regions with moderate to high SST variability, spatial scales of order 100 km tend to strengthen a positive correlation. At small scales that are similar to the grid size, the sign of the sensible heat flux is opposite to the local SST anomaly, which leads to a negative correlation between SST and wind speed. This is likely the case in the Atlantic region.

b. *In situ data*

The gridded data products discussed above have the advantage of nearly global coverage and uniform spacing. However, the resolution of 0.25° is often too coarse to resolve ocean eddies, and, therefore, the coupling between OBL and ABL implied from these datasets might be somewhat underestimating the true signals. Furthermore, the gridded wind product is a remotely sensed indirect observation more directly related to wind stress than to speed. To estimate any effect these limitations might have, we repeat the above analysis with in situ buoy data within the Pacific and Atlantic regions. In the Pacific, the results are nearly identical, except the wind speed fluctuations observed at the buoys have smaller values and their distributions are slightly narrower (Fig. 6). Note that the gridded data represent equivalent neutral wind speed at 10-m height, whereas the buoy data are observations at about 5-m height.

In the Atlantic region, the SST fluctuations are significantly larger in the in situ observations, ΔSST = ±5 K (Fig. 7), compared to the gridded blended remote sensing data, for which ΔSST = ±2.5 K. The range of the mean wind speed fluctuations is similar in both datasets, and the extreme values are slightly lower in the buoy observations. More importantly, the correlations between SST and wind speed are weaker in the buoy data, but they do support the predominance of thermal coupling found in the gridded dataset.

The values and overall dependencies of the slope of the linear fit p_{mean} are shown in Fig. 8. For the Pacific region, results are consistent between the gridded data and the buoy data. In the Atlantic, there are several differences between the two datasets. Since the range of SST fluctuations is generally larger in the in situ observations, the magnitude of the slopes is smaller in the buoy observations, even if corrected for the reduced height of the wind observations. Only data from SON indicate mechanical coupling (i.e., $p_{\text{mean}} < 0$ for $\tau < 0$), whereas the gridded data also included JJA in this regime. Similarly, during the summer season, the dominance of the extreme wind speed fluctuations in the mechanical coupling ($\tau < 0$) is much stronger in the buoy data, compared to the gridded data ($|p_{95\text{prct}}(\text{buoy})| < |p_{95\text{prct}}(\text{grid})|$ and $\Delta\text{SST} \propto p_{95\text{prct}}^{-1}\Delta U_{95\text{prct}}$). In conclusion, we find that the buoy observations confirm the results from the gridded data in qualitative terms. However, the dynamic range of the SST fluctuations is smaller in the gridded data, likely because the 0.25° resolution of the satellite data smears out some small-scale eddy structure.

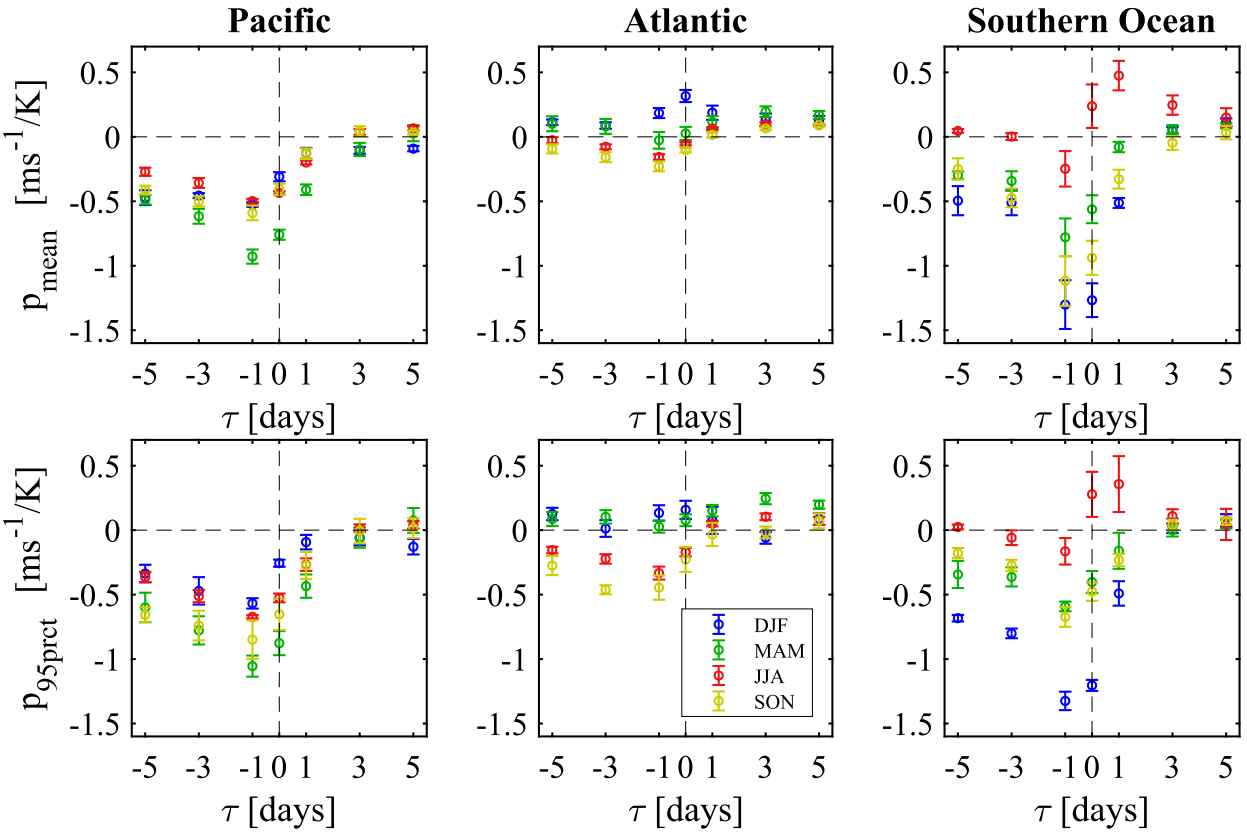

FIG. 5. Slope of linear fit through wind speed anomalies as function of SST anomalies from gridded data products in the (left) northeast Pacific, (center) northwest Atlantic, and (right) Southern Ocean as function of lag τ. Error bars represent 95% confidence levels for (top) anomaly of the mean wind speed and (bottom) anomalies of the 95th percentile of wind speed fluctuations.

Seasonal averages of the buoy observations of air–sea temperature difference θ, SST, wind speed, and direction of the mean vector wind dd, as well as the mean standard deviations, are given in Table 1. The Atlantic region is dominated by westerly wind, whereas in the Pacific region, the dominant wind regime is more southwesterly, but mean wind speeds are comparable. These mean wind directions are very persistent: the fractions p_{dd} of wind observations deviating by more than 90° from the mean direction are $0.18 \leq p_{dd} \leq 0.28$. The Pacific region has a strong variability in air temperature, especially in winter and spring, $\sigma(T_a) > 7\,\mathrm{K}$, but little variability in SST, $\sigma(\mathrm{SST}) \leq 1.3\,\mathrm{K}$. The SST variability in the Atlantic region is consistently higher, $\sigma(\mathrm{SST}) \approx 2.3\,\mathrm{K}$, with no seasonal variations. Another significant difference between these regions is the mean air–sea temperature difference: in the Pacific $|\theta| < 1\,\mathrm{K}$, but it reaches $\theta = -2.6\,\mathrm{K}$ in DJF in the Atlantic.

4. Stochastic model

A key finding from our analysis of the observations is that the coupling between the oceanic and the atmospheric boundary layers at the oceanic mesoscale can be either mechanically or thermally dominated. Indications are that if strong eddy-induced SST fluctuations are present, the OBL drives the lower atmosphere, as seen in the Atlantic region. In the absence of strong internal SST fluctuations, the OBL merely responds to its mechanical coupling with the ABL, which is the dominant effect in the Pacific and the Southern Ocean regions.

To test this working hypothesis, and to determine the importance of the different coupling terms, we set up an idealized 1D coupled model of the momentum and heat budgets in the oceanic and atmospheric boundary layers. Exchange processes between the two boundary layers aiming at equilibration of the heat budget are largely driven by turbulence, which, in turn, is influenced by the thermal stratification (i.e., the degree of nonequilibrium). In addition, the ABL has a much shorter time scale of equilibration than the OBL. As such, the coupled system can be framed in terms of a stochastic model for the evolution of momentum and heat (Monahan and Culina 2011). The model is formulated as deviations from a mean state, and fluctuations on synoptic time scales representing "weather" are included as stochastic processes.

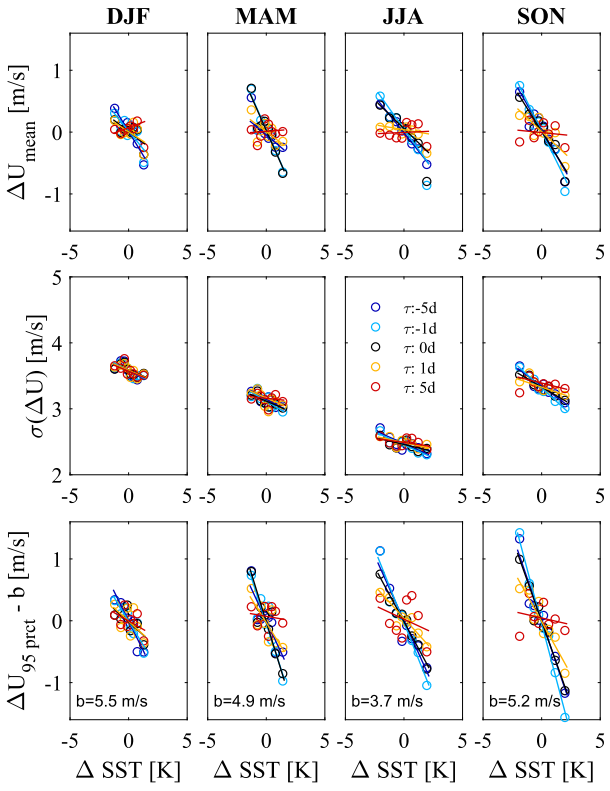

FIG. 6. As in Fig. 2, but for buoy observations in the northeast Pacific.

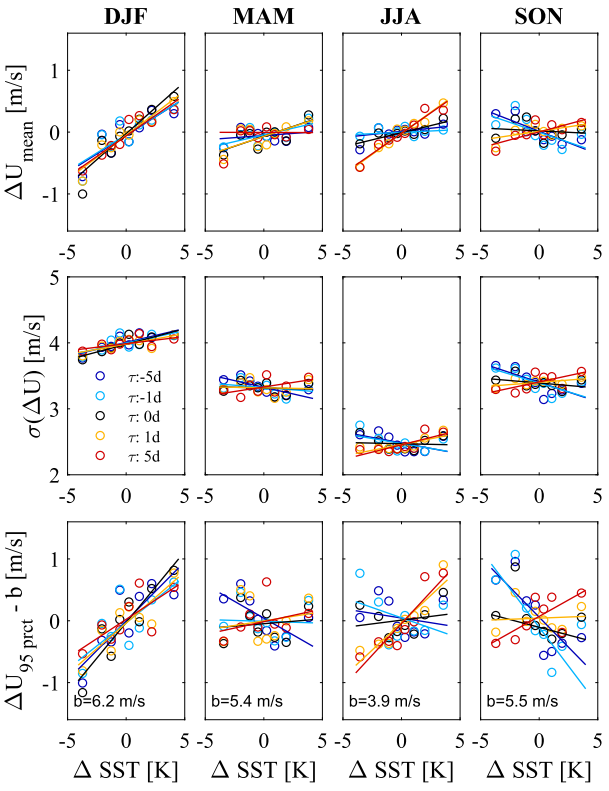

FIG. 7. As in Fig. 6, but for the northwest Atlantic.

Here, we separate the governing equations for momentum into two parts, concerning (i) random fluctuations in the pressure gradient force, expressed as the equivalent geostrophic wind and modeled as a red noise process:

$$\frac{du_g}{dt} = -\frac{u_g}{\tau_c} + \frac{\sigma}{\tau_c}\dot{W}_1, \quad \text{and} \tag{1}$$

$$\frac{dv_g}{dt} = -\frac{v_g}{\tau_c} + \frac{\sigma}{\tau_c}\dot{W}_2; \tag{2}$$

and (ii) the resulting wind, subject to momentum exchange at the top of ABL and with the underlying OBL:

$$\frac{du}{dt} = \Pi_u - fv_g - \frac{C_d u_h}{H}u - \frac{w_e}{H}u, \quad \text{and} \tag{3}$$

$$\frac{dv}{dt} = fu_g - \frac{C_d u_h}{H}v - \frac{w_e}{H}v, \tag{4}$$

with (u_g, v_g) geostrophic wind component deviations, τ_c decorrelation time scale, $\sigma = \sigma_{ug}(2\tau_c)^{1/2}$, σ_{ug} standard deviation of the geostrophic wind speed, $\dot{W}_{1,2}$ independent Gaussian white noise processes, Π_u mean acceleration associated with the mean pressure gradient, f Coriolis parameter, C_d drag coefficient, $u_h = (u^2 + v^2)^{1/2}$ wind speed, and w_e entrainment velocity at the top of the ABL. The depth of the ABL depends on the stratification $H = [1 + \alpha(T_a - T_w)]H_{\text{mean}}$, where T_a and T_w are temperature of the air and water side, respectively, and the empirical coefficient $\alpha = -0.14\ \text{K}^{-1}$ represents the variability of the ABL height due to production/consumption of turbulence kinetic energy (Monahan and Culina 2011).

The linearized governing equations for heat, formulated in terms of temperature deviations T_a, T_w, are

$$\frac{dT_a}{dt} = A_h\left[\frac{\beta}{\gamma_a}(T_w - T_a)u_h - \frac{\beta}{\gamma_a}\theta(u_h - \overline{u}_h)\right] - \frac{\lambda_a}{\gamma_a}T_a + \Gamma_{11}\dot{W}_3 + \Gamma_{12}\dot{W}_4, \tag{5}$$

$$\frac{dT_w}{dt} = \frac{\beta}{\gamma_w}(T_a - T_w)u_h + \frac{\beta}{\gamma_w}\theta(u_h - \overline{u}_h) - \frac{\lambda_w}{\gamma_w}T_w + \Gamma_{21}\dot{W}_3 + \Gamma_{22}\dot{W}_4 + \Delta T_{\text{eddy}} + A\frac{\Theta_{\text{ML}}}{\Delta H_w}, \tag{6}$$

where $\gamma_a = c_{p_a}\rho_A H$ and $\gamma_w = c_{p_w}\rho_w H_w$, and $H_w = H_w(t)$ is the depth of the OBL, $\overline{u}_h$ is the mean wind speed, c_{p_a}, c_{p_w} are the specific heat capacity, and ρ_a, ρ_w are the density of air and water, respectively (Barsugli and Battisti 1998). The net exchange coefficient $\beta = \rho_a c_p C_H(1 + B)$;

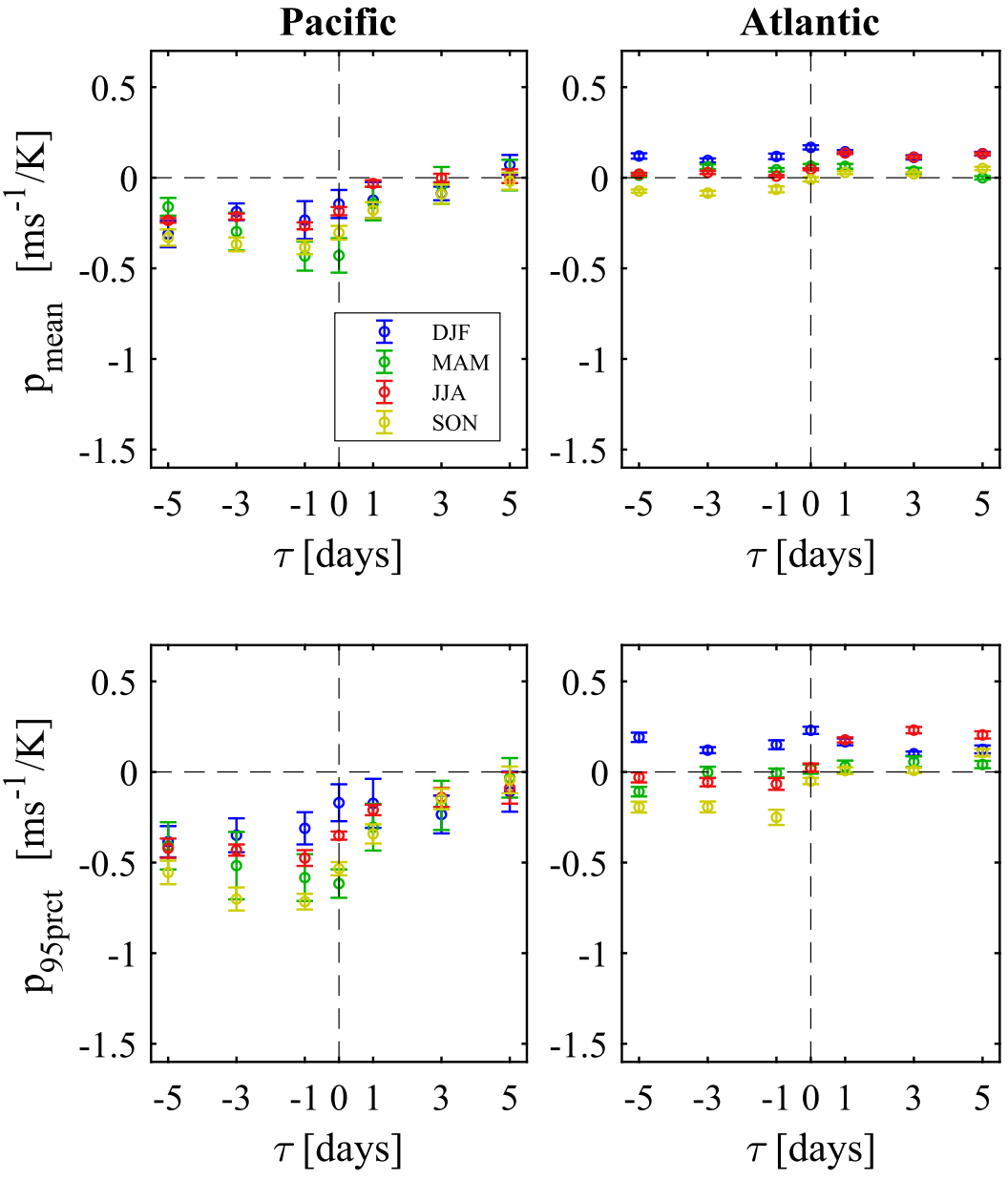

FIG. 8. Slope of linear fit through wind speed anomalies as function of SST anomalies from buoy observations in the (left) northeast Pacific and (right) northwest Atlantic as function of lag τ. Error bars represent 95% confidence levels for (top) anomaly of the mean wind speed and (bottom) anomalies of the 95th percentile of wind speed fluctuations.

where C_H is the bulk exchange coefficient for sensible heat and B is the Bowen ratio. The mean air–sea temperature difference, resulting in a mean heat flux, is θ, and the mean temperature difference between the OBL and the underlying ocean is Θ_{ML}. Here, we include the factor A_h, with $0 < A_h \leq 1$ to account for a slower thermal adjustment of the atmospheric column due to lateral advection, which cannot explicitly be resolved in a 1D model. The relaxation time scales by which temperature fluctuations adjust to the mean state are defined by the coefficients λ_a and λ_w for the atmosphere and ocean, respectively. The terms involving $\Gamma_{ij}\dot{W}_k$ are independent white noise processes representing unresolved fast fluctuations of the heat budget (e.g., variable cloudiness, humidity, wind gustiness, and small-scale oceanic processes, such as wave breaking, Langmuir mixing, and surface currents). We introduced the last two terms in (6) to specifically allow for external temperature fluctuations ΔT_{eddy} due to mesoscale eddies and due to the entrainment associated with a change in the mixed layer depth ΔH_w.

TABLE 1. Seasonal values derived from buoy observations in the Pacific and Atlantic regions. Parameter θ is air–sea temperature difference, SST is sea surface temperature, T_a is air temperature, U is wind speed, dd is direction of the mean vector wind, σ is standard deviation, and p_{dd} is fraction of wind observations opposing the mean direction.

Month	θ (K)	SST (°C)	U (m s^{-1})	dd (°N)	σ(SST) (K)	$\sigma(T_a)$ (K)	$\sigma(U)$ (m s^{-1})	p_{dd}
				Pacific				
DJF	0.44	7.3	8.7	214	0.88	7.09	3.58	0.28
MAM	0.95	7.1	7.3	221	0.94	7.20	3.15	0.28
JJA	−0.36	12.5	6.0	260	1.30	1.32	2.48	0.18
SON	−0.74	12.1	8.2	244	1.26	2.30	3.35	0.18
				Atlantic				
DJF	−2.61	6.9	8.8	287	2.36	5.40	4.00	0.19
MAM	0.73	6.0	6.9	268	2.26	6.97	3.34	0.25
JJA	0.59	16.1	5.2	228	2.25	5.15	2.47	0.20
SON	−1.43	15.1	7.2	283	2.29	4.57	3.38	0.24

Adjustment of the mixed layer depth ΔH_w is based on the balance between available kinetic energy and the change of potential energy due to the entrainment of denser water from the layers below. Here, we define available kinetic energy:

$$\Delta \mathrm{KE} = E_{\mathrm{in}} - E_{\mathrm{dis}}. \tag{7}$$

It is the difference of the energy input by the wind $E_{\mathrm{in}} \propto c_{\mathrm{eff}}\, u_*^2$ (Gemmrich et al. 1994), with u_* the friction velocity in water and c_{eff} the effective phase speed of energy acquiring waves, and a fixed dissipation rate E_{dis} representing the combined effect of viscous and turbulent dissipation in the upper ocean.

In the case of $\Delta \mathrm{KE} > 0$, the mixed layer deepens until a balance with the change in potential energy,

$$\Delta \mathrm{PE} = \gamma^{-1} \sum (\alpha_w g \Theta_{\mathrm{ML}} \Delta z), \tag{8}$$

is achieved, where Σ is the summation over the depth layers. The deepening is calculated iteratively in depth increments Δz, and the temperature in the entire OBL is adjusted instantaneously to be uniform. The total change in OBL depth is $\Delta H_w = \Sigma(\Delta z)$. In the case of $\Delta \mathrm{KE} \le 0$, the mixing layer shoals to a level where the depth-integrated background dissipation and energy input match. In the case that an unstable temperature profile is generated, this is removed by instantaneous mixing at the end of each time step.

The effects of external ocean eddies are modeled as slow temperature modulations in the entire OBL:

$$T_{\mathrm{eddy}}(t) = c_E T_E \sin(n\pi \Delta t/\tau_{\mathrm{eddy}}), \tag{9}$$

where T_E is the maximum temperature deviation within the eddy, and $-1 \le c_E \le 1$ is a random variable allowing for cold and warm eddies and peripheral eddy passage. Each eddy has a duration τ_{eddy}, which is drawn randomly from a range of $0.8\tau_E \le \tau_{\mathrm{eddy}} \le 1.2\tau_E$ and is reinitialized at time step $n = \tau_{\mathrm{eddy}}/\Delta t$.

This model includes three coupling processes between the atmosphere and the ocean: (i) wind speed anomalies modulate air and water temperature via modified air–sea heat fluxes, and (ii) water temperature via the change in OBL mixing layer depth; (iii) fluctuations in air temperature and water temperature affect the atmospheric momentum budget via the adjustment of the ABL depth. The change of horizontal pressure gradients, which could also modulate the atmospheric momentum, is not explicitly included in this 1D model.

a. Nondimensional model equations

The dominant features of this model are best highlighted in a nondimensional form of the above-stated equations. The scaling parameters used are the time scale of ABL adjustment τ_a, the standard deviation of geostrophic wind speed σ_g, the average ABL depth H_m, and an arbitrary scaling parameter for temperature anomalies T_m, that is, $\tilde{u} = u/\sigma_g$, $\tilde{T} = T/T_m$, $\tilde{t} = t/\tau$, $\tilde{H} = H/H_m$.

With this scaling, the model equations reduce to

$$\frac{d\tilde{u}_g}{d\tilde{t}} = A_1 \tilde{u}_g + A_{12} \tilde{W}_1, \tag{10}$$

$$\frac{d\tilde{v}_g}{d\tilde{t}} = A_1 \tilde{v}_g + A_{12} \tilde{W}_2, \tag{11}$$

$$\frac{d\tilde{u}}{d\tilde{t}} = B_0 - B_1 \tilde{v}_g - B_2 \tilde{u}_h \frac{\tilde{u}}{\tilde{H}} - B_3 \frac{\tilde{u}}{\tilde{H}}, \tag{12}$$

$$\frac{d\tilde{v}}{d\tilde{t}} = B_1 \tilde{u}_g - B_2 \tilde{u}_h \frac{\tilde{v}}{\tilde{H}} - B_3 \frac{\tilde{v}}{\tilde{H}}, \tag{13}$$

$$\frac{d\tilde{T}_a}{d\tilde{t}} = C_1 \left[\frac{\tilde{u}_h}{\tilde{H}} (\tilde{T}_w - \tilde{T}_a) - \frac{\tilde{u}_h - \tilde{U}}{\tilde{H}} \tilde{\theta} \right] - C_2 \tilde{T}_a + C_{31} \dot{W}_3 + C_{32} \dot{W}_4, \quad \text{and} \tag{14}$$

$$\frac{d\tilde{T}_w}{d\tilde{t}} = C_{1w}\left[\frac{\tilde{u}_h}{\tilde{H}_w}(\tilde{T}_a - \tilde{T}_w) + \frac{\tilde{u}_h - \tilde{U}}{\tilde{H}_w}\tilde{\theta}\right] - C_{2w}\tilde{T}_w + C_{31w}\dot{W}_3 + C_{32w}\dot{W}_4 + \Delta\tilde{T}_{\text{eddy}} + A\frac{\tilde{\Theta}_{ML}}{\Delta\tilde{H}_w}, \quad (15)$$

where the model parameters are now ratios of relevant time scales:

$$A_1 = -\frac{\tau_a}{\tau_c};$$

$$B_0 = \frac{\tau_a}{\sigma_g/\Pi_u}; \quad B_1 = \frac{\tau_a}{1/f}; \quad B_2 = -\frac{\tau_a}{H_m/(C_d\sigma_g)};$$

$$B_3 = \frac{w_e}{C_d\sigma_g}B_2$$

$$C_1 = A_h\frac{\tau_a}{H_m/[\sigma_g C_H(1+B)]}; \quad C_2 = 1; \quad C_{1w} = \frac{\rho c_p}{\rho_w c_w}\frac{C_1}{A_h};$$

$$C_{2w} = \frac{\tau_a}{\tau_w}; \quad (16)$$

and

$$A_{12} = (2A_1)^{1/2}; \quad \tilde{W}_n = \dot{W}_n/\tau_a^{1/2},$$

$$C_{31} = \frac{\tau_a}{T_m/\Gamma_{11}}; \quad C_{32} = \frac{\tau_a}{T_m/\Gamma_{12}} \quad C_{31w} = C_{31}\frac{\Gamma_{21}}{\Gamma_{11}};$$

$$C_{32w} = C_{32}\frac{\Gamma_{22}}{\Gamma_{12}}; \quad (17)$$

$$\tilde{H} = \max\left[1 + \alpha T_m(\tilde{T}_a - \tilde{T}_w), \tilde{H}_{\min}\right]. \quad (18)$$

b. Model results

The model is run such that for each parameter setting, an ensemble of 20 realizations of 3-yr duration is generated. The full-resolution time series of wind components and air and water temperature anomalies are then averaged over a 1-day period to match the sampling rate and resolution of the gridded observational data. There is no seasonality included in the model, and thus, the dependencies between wind speed fluctuations and SST fluctuations are calculated from the entire records. However, the models are run for different mean air–sea temperature differences θ, which can be regarded as a proxy for seasonal variations.

The model is intended for extracting key processes, rather than for making quantitatively accurate predictions. Nevertheless, all model parameters are chosen from a range of realistic values, and all physical constants are those of air or saltwater. In the following analysis, the relevance of OBL temperature modulations by (i) oceanic eddy activity and (ii) entrainment of colder water from below the OBL are tested.

TABLE 2. Values of nondimensional model parameters [Eqs. (16) and (17)] associated with the results shown in Figs. 9 and 10.

A_1	B_0	B_1	B_2	B_3	C_1	C_{1w}	C_2	C_{2w}
0.071	0.270	4.320	0.026	0.054	0.044	1.3×10^{-4}	1.000	0.150
A_{12}	C_{31}	C_{31w}	C_{32}	C_{32w}	T_E	τ_E		
0.378	0.112	−0.002	0.002	0.008	[0,1,5]	10		

An illustrative example for a nondimensional model run (Table 2) with moderate eddy activity corresponding to $T_{\text{eddy}} = 1$ K, $\tau_{\text{eddy}} = 10$ d, and variable OBL depth is shown in Fig. 9. In this case, the nature of the dominant coupling depends on the mean air–sea temperature difference. The sign of the response follows the sign of the mean air–sea temperature difference θ, and atmosphere-driven ($\tau < 0$, blue symbols) and ocean-driven coupling ($\tau > 0$, red symbols) generally have opposite ΔSST–ΔU_{mean} correlations. For conditions with air being colder than the water, $\theta < 0$, there is a negative correlation between wind and SST fluctuations for $\tau < 0$: positive wind fluctuations lead to reduction in SST, mainly due to sensible heat exchange and, to a smaller extent, due to entrainment of colder water. A corresponding simulation with fixed OBL depth shows qualitatively the same behavior but with smaller amplitudes, suggesting that heat flux modulations are the dominant factor in decreasing SST. Weaker winds reduce the heat flux and, thus, result in a positive SST anomaly. For $\tau \geq 0$, the correlation is positive but smaller. During stable conditions, $\theta > 0$, the system is mainly thermally driven, $\tau > 0$, and positive (negative) SST anomalies lead to positive (negative) wind speed anomalies. For neutral conditions, $\theta = 0$, the effects of mechanical (blue symbols) and thermal (red symbol) coupling have roughly the same strength and opposite sign.

The observations reveal both positive and negative conditional dependencies of wind speed on SST fluctuations, mainly depending on whether the system is thermally or mechanically driven. The idealized 1D model is capable of reproducing these different regimes. For example, the run shown in Fig. 9 includes the positive feedback of SST on wind speed for $\theta > 0$, $\tau > 0$, as well as the effect of wind speed fluctuations on SST for $\tau \leq 0$. We utilized the model to map out the relative importance of these coupling processes. The model was run with the same basic model parameters (Table 2) and (i) fixed OBL depth and no prescribed eddies, (ii) dynamic OBL depth and no eddies, (iii) fixed OBL depth and strong prescribed

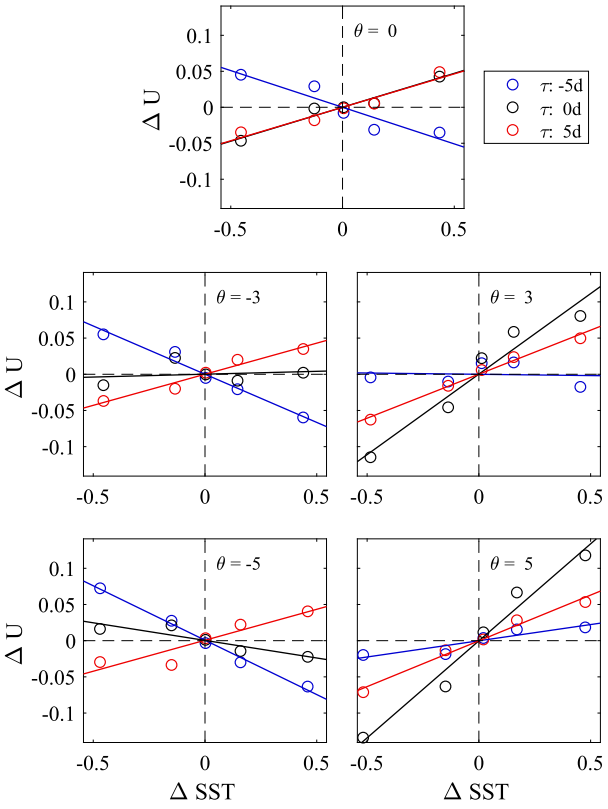

FIG. 9. Wind speed anomalies as function of SST anomalies as obtained from the 1D nondimensional model. Individual data (circles) and least squares fit (line) are given for different lags. Each panel represents a different mean air–sea temperature difference θ, stated on the figure.

eddy-associated SST fluctuations, and (iv) a dynamic OBL depth and strong eddy activities. The results are summarized in Fig. 10. The red symbols show the mean wind speed anomalies associated with the 5% largest positive SST anomalies, and the blue symbol shows the 5% largest negative SST anomalies as function of time lag τ.

In the case where the SST is not modulated by external eddies (first two columns in Fig. 10), the SST fluctuations are governed by the mean air–sea temperature difference, with positive (negative) temperature anomalies associated with positive (negative) wind anomalies for air temperature being greater than the mean SST, $\theta > 0$, and the opposite relationship for $\theta < 0$. In the case of neutral stratification, $\theta = 0$, entrainment at the bottom of the OBL is the only mechanism to generate SST anomalies, and for wind leading SST, $\tau < 0$, an increased (reduced) wind speed yields a cooling (warming) of the OBL. There is very little response at $\tau > 0$. Weak eddy activity, $T_E = 1$, results in larger SST anomalies but does not alter the overall OBL–ABL coupling response, compared to the cases with no eddies (Fig. 9). The cases with near-neutral stratification ($|\theta| < 1$ K) and weak intrinsic SST fluctuations (Fig. 10, middle of second column) are representative for the condition in the Pacific (Fig. 2, Table 1).

In the case of strong SST modulation, $T_E = 5$ (last two columns in Fig. 10), warmer (colder) SST leads to an increased (reduced) wind speed, independent of the mean air–sea temperature difference, although the signal is strongest for stable conditions, $\theta > 0$. For $\tau < 0$ (i.e., wind fluctuations leading SST fluctuations), the coupling is due to modulated heat fluxes, and the response is qualitatively similar to the cases with no eddy activity. In our model setup, the temperature modulations due to eddies are depth independent within the OBL and dominate SST changes due to entrainment. Therefore, model runs with dynamic OBL depth give nearly identical results as runs with a fixed OBL depth. Model runs for strong eddy activity and negative or near-neutral air–sea temperature differences (Fig. 10, bottom right and middle right) are representative of the most common conditions in the Atlantic (Figs. 3, 7, columns 2–4). However, the counterintuitive result of a positive covariability of wind fluctuations leading SST anomalies observed during DJF in the Atlantic (Figs. 3, 7, column 1) is not captured in our model.

5. Conclusions

The observations reveal two different regimes of the link between wind speed and SST fluctuations, based on the relative dominance of the physical processes involved in the coupling between ABL and OBL. This leads to conditions where (i) fluctuations in SST affect the stability and depth of the overlying ABL and therefore a positive correlation between SST fluctuations and the statistics of wind speed fluctuations, and (ii) where fluctuations in wind speed generate SST fluctuations due to enhanced air–sea heat fluxes and entrainment of colder water at the thermocline. The two regimes can result in opposite responses. The Atlantic region is in an area of strong eddy activity, and the coupling is mainly driven from the ocean side due to eddy-related SST fluctuations of up to 5 K. For example, an increase in SST will lead, on average, to an increase in wind speed. This process is present throughout all seasons but is strongest in winter (Figs. 3, 7; $\tau > 0$). On the other hand, the Pacific region and the Southern Ocean are areas without strong SST variations associated with internal ocean eddy dynamics. In these regions, SST fluctuations are mainly associated with wind fluctuations; that is, the wind is leading SST (Figs. 2, 6, 4; $\tau \leq 0$). In both regions, positive wind speed fluctuations are

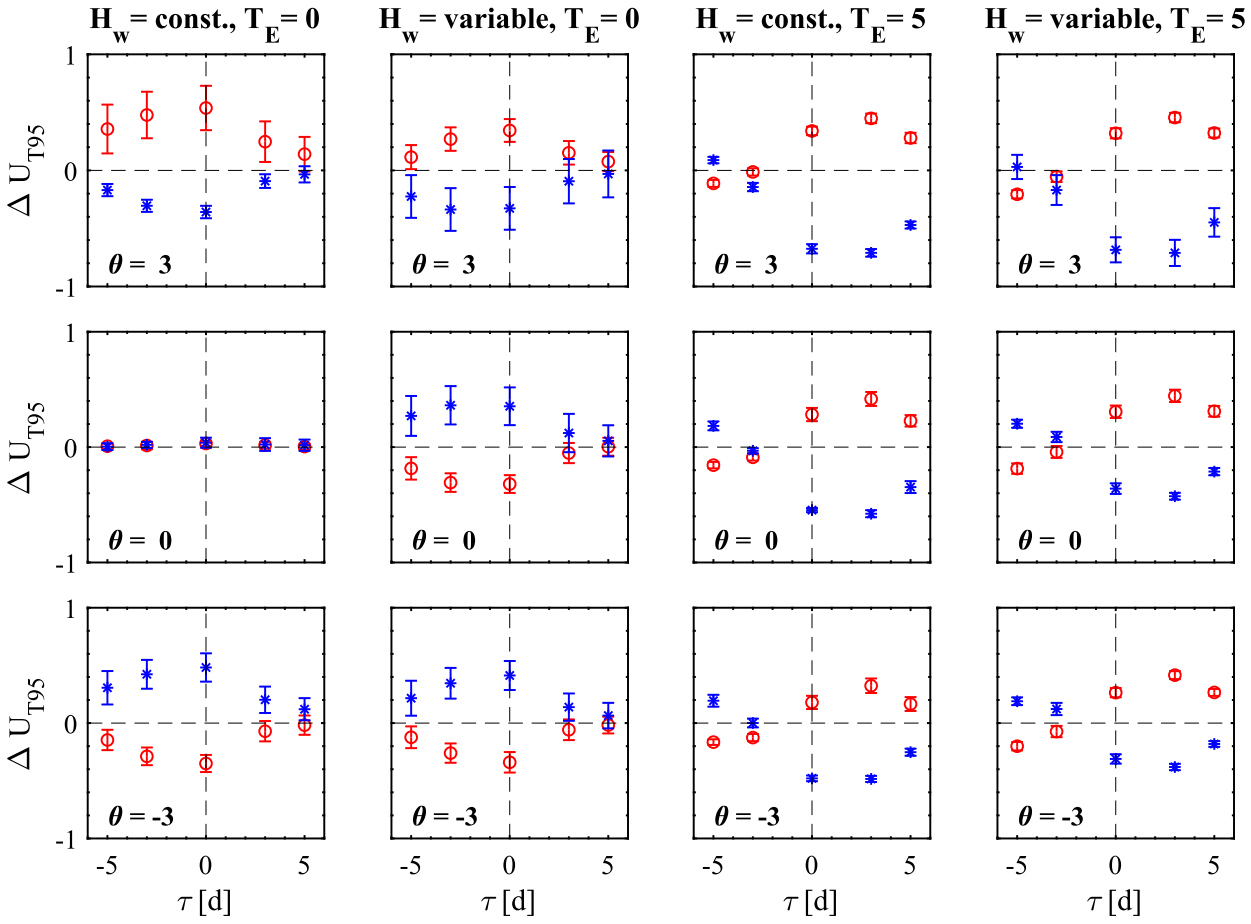

FIG. 10. Wind speed anomalies ΔU_{T95} associated with the 5% largest positive (red) and negative (blue) temperature anomalies ΔT_{95} from the 1D nondimensional model as function of time lag τ and mean air–sea temperature difference θ. Columns represent different model configurations for OBL depth H_W and inclusion of ocean eddies ($T_E \neq 0$), with all other model parameters kept the same (see Table 1).

associated with negative SST anomalies. This can be achieved by an increased upward heat flux or by entrainment at the bottom of the OBL. Air–sea temperature differences are close to zero, and latent heat is the largest contributor to the air–sea heat flux. Wind speed is positively correlated with entrainment, which, in turn, has a negative correlation with SST. Thus, the negative wind speed–SST correlation can be a combination of modulated latent heat flux and entrainment. The physical origin of positive SST–ΔU correlations for negative lags for DJF in the Atlantic remains unclear and is an interesting direction for future research.

The model results can be summarized in two key findings. In the absence of strong air–sea temperature difference (e.g., the eastern North Pacific or the Southern Ocean), it is essential to include the depth variability of the OBL to properly represent the relationship between SST and wind speed variations (Fig. 10, middle row). The second finding concerns the importance of eddy-related SST fluctuations. Eddies with moderate temperature anomalies do not alter the principal tendencies of the coupling. However, eddy-associated SST fluctuations of a few centigrade can dominate over the SST anomalies generated by changes in air–sea heat flux or entrainment at the bottom of the OBL. These strong eddies can change the ABL–OBL coupling to a thermally driven system, even at spatial scales of a few tens of kilometers. Our model results suggest that the inclusion of ocean eddies in coupled models is crucial: moderate eddy SST anomalies can have a significant effect on extreme wind speed anomalies, whereas strong eddy SST anomalies can switch the coupling from a mechanically dominated to a thermally driven system, with opposite ΔSST–ΔU response. A similar fundamental difference in mesoscale air–sea coupling is expected close to and away from strong thermal fronts.

Acknowledgments. This work was supported by the Canadian Networks of Centres of Excellence as part of Marine Environmental Observation, Prediction and

Response (MEOPAR). AHM acknowledges support from the Natural Sciences and Engineering Research Council (NSERC) of Canada. Gridded SST and wind data were obtained from the NASA EOSDIS Physical Oceanography Distributed Active Archive Center (PO.DAAC). Buoy data are provided by Fisheries and Oceans Canada (http://www.meds-sdmm.dfo-mpo.gc.ca).

REFERENCES

Alexander, M., and C. Penland, 1996: Variability in a mixed layer ocean model driven by stochastic atmospheric forcing. *J. Climate*, **9**, 2424–2442, https://doi.org/10.1175/1520-0442(1996)009<2424:VIAMLO>2.0.CO;2.

Barsugli, J., and D. Battisti, 1998: The basic effects of atmosphere–ocean thermal coupling on midlatitude variability. *J. Atmos. Sci.*, **55**, 477–493, https://doi.org/10.1175/1520-0469(1998)055<0477:TBEOAO>2.0.CO;2.

Bishop, S. P., R. J. Small, F. O. Bryan, and R. A. Tomas, 2017: Scale dependence of midlatitude air–sea interaction. *J. Climate*, **30**, 8207–8221, https://doi.org/10.1175/JCLI-D-17-0159.1.

Cavaleri, L., and Coauthors, 2007: Wave modelling—The state of the art. *Prog. Oceanogr.*, **75**, 603–674, https://doi.org/10.1016/j.pocean.2007.05.005.

Chelton, D., and S.-P. Xie, 2010: Coupled ocean–atmosphere interaction at oceanic mesoscales. *Oceanography*, **23** (4), 52–69, https://doi.org/10.5670/oceanog.2010.05.

Fairall, C. W., E. F. Bradley, J. E. Hare, A. A. Grachev, and J. B. Edson, 2003: Bulk parameterization of air–sea fluxes: Updates and verification for the COARE algorithm. *J. Climate*, **16**, 571–591, https://doi.org/10.1175/1520-0442(2003)016<0571:BPOASF>2.0.CO;2.

Frankignoul, C., 1985: Sea surface temperature anomalies, planetary waves, and air-sea feedback in the middle latitudes. *Rev. Geophys.*, **23**, 357–390, https://doi.org/10.1029/RG023i004p00357.

Gaube, P., D. B. Chelton, R. M. Samelson, M. G. Schlax, and L. W. O'Neill, 2015: Satellite observations of mesoscale eddy-induced Ekman pumping. *J. Phys. Oceanogr.*, **45**, 104–132, https://doi.org/10.1175/JPO-D-14-0032.1.

Gemmrich, J. R., T. D. Mudge, and V. D. Polonichko, 1994: On the energy input from wind to surface waves. *J. Phys. Oceanogr.*, **24**, 2413–2417, https://doi.org/10.1175/1520-0485(1994)024<2413:OTEIFW>2.0.CO;2.

Hasselmann, K., 1976: Stochastic climate models. Part I: Theory. *Tellus*, **28**, 473–485, https://doi.org/10.3402/tellusa.v28i6.11316.

Liu, G., W. Perrie, V. Kudryavtsev, Y. He, H. Shen, B. Zhang, and H. Hu, 2016: Radar imaging of intense nonlinear Ekman divergence. *Geophys. Res. Lett.*, **43**, 9810–9818, https://doi.org/10.1002/2016GL070799.

Monahan, A. H., and J. Culina, 2011: Stochastic averaging of idealized climate models. *J. Climate*, **24**, 3068–3088, https://doi.org/10.1175/2011JCLI3641.1.

Perry, K., 2001: SeaWinds on QuikSCAT Level 3 daily, gridded ocean wind vectors (JPL SeaWinds Project). JPL Tech. Rep. D-20335, 39 pp., https://doi.org/10.5067/QSXXX-L3002.

Renault, L., M. Molemaker, J. McWilliams, A. F. Shchepetkin, F. Lemarié, D. Chelton, S. Illig, and A. Hall, 2016: Modulation of wind work by oceanic current interaction with the atmosphere. *J. Phys. Oceanogr.*, **46**, 1685–1704, https://doi.org/10.1175/JPO-D-15-0232.1.

Reynolds, R. W., T. M. Smith, C. Liu, D. B. Chelton, K. S. Casey, and M. G. Schlax, 2007: Daily high-resolution-blended analyses for sea surface temperature. *J. Climate*, **20**, 5473–5496, https://doi.org/10.1175/2007JCLI1824.1.

Sampe, T., and S.-P. Xie, 2007: Mapping high sea winds from space: A global climatology. *Bull. Amer. Meteor. Soc.*, **88**, 1965–1978, https://doi.org/10.1175/BAMS-88-12-1965.

Schulz, E., S. A. Josey, and R. Verein, 2012: First air-sea flux mooring measurements in the Southern Ocean. *Geophys. Res. Lett.*, **39**, L16606, https://doi.org/10.1029/2012GL052290.

Seo, H., 2017: Distinct influence of air–sea interactions mediated by mesoscale sea surface temperature and surface current in the Arabian Sea. *J. Climate*, **30**, 8061–8080, https://doi.org/10.1175/JCLI-D-16-0834.1.

Shaman, J., R. M. Samelson, and E. Skyllingstad, 2010: Air–sea fluxes over the Gulf Stream region: Atmospheric controls and trends. *J. Climate*, **23**, 2651–2670, https://doi.org/10.1175/2010JCLI3269.1.

Small, R. J., and Coauthors, 2008: Air–sea interaction over ocean fronts and eddies. *Dyn. Atmos. Oceans*, **45**, 274–319, https://doi.org/10.1016/j.dynatmoce.2008.01.001.

Yu, L., and R. A. Weller, 2007: Objectively analyzed air–sea heat fluxes for the global ice-free oceans (1981–2005). *Bull. Amer. Meteor. Soc.*, **88**, 527–539, https://doi.org/10.1175/BAMS-88-4-527.